Interfacial anisotropy in the transport of liquid crystals confined between flat, structureless walls: A molecular dynamics simulation approach

Toshiki Mima* and Kenji Yasuoka
Department of Mechanical Engineering, Keio University, Yokohama 223-8522, Japan
(Received 29 June 2007; revised manuscript received 13 November 2007; published 22 January 2008)

Molecular dynamics simulations of uniaxial Gay-Berne ellipsoids as prolate liquid crystal molecules confined between two flat, structureless walls have been carried out in order to investigate anisotropy in their dynamic properties. Several physical quantities are profiled as a function of distance from a wall. The walls stimulate ellipsoids into different behaviors from those of the bulk system. The profiles of self-diffusion coefficients, which are distinguished in each direction of a director-based coordinate system, show that the ellipsoids are more diffusive parallel to the walls and less diffusive perpendicular to the walls with decreasing distance from the walls. According to the self-rotation coefficient and rotational viscosity profiles, ellipsoids are easy to rotate parallel to the walls and hard to rotate in the plane perpendicular to the walls. The analyses of velocity autocorrelation functions, angular velocity autocorrelation functions, director angular velocity autocorrelation functions, and their spectra are useful for the investigation of anisotropy near the walls. We conclude that the flat, structureless wall not only prevents ellipsoids from diffusing and rotating in the plane perpendicular to the walls, but also stimulates them to diffuse and rotate in the plane parallel to the walls.

DOI: 10.1103/PhysRevE.77.011705 PACS number(s): 61.30.Cz, 47.57.Lj, 68.08.−p

I. INTRODUCTION

With the recent development of microfabrication techniques, research into the properties of molecules confined in submicron- or nano-sized devices is necessary. Confined molecules generally show different characteristics from those in bulk systems [1]. Soft matters in submicron pores or nanopores have also been investigated using nuclear magnetic resonance methods. Jin *et al.* confined liquid crystal molecules of cyanobiphenyl series in porous almina and investigated the anchoring transition dependent on the length of the hydrocarbon tail of the liquid crystal [2]. Zax *et al.* researched the mobility of a polymer confined in a slit pore of a few nanometers width [3].

Simulational approaches are also useful for investigating molecules confined in nanosized devices. The thermodynamics of particles in a partially closed environment demands that the volume is decomposed into two variables: one characteristic to the system and another that is not [4]. For instance, the volume can be decomposed into the distance between two walls and the rest of the surface area when particles are confined between a slit-pore; then the thermodynamic variables of the cylindrical system are the radius and the length of the cylinder. Molecules confined in a slit [5–10], a cylinder [11–16], and a nanoporous material [17] have been investigated widely with molecular dynamics simulation, Monte Carlo simulation, and so on.

Liquid crystal molecules realize several intermediate phases, depending on the shapes of each molecule and they have been utilized in display technology. Liquid crystal molecules confined in nanopore shapes are expected to be applied devices and they have been investigated by molecular dynamics simulations and Monte Carlo simulations in the last decade. Wall and Cleaver carried out molecular dynamics simulations of prolate uniaxial ellipsoids confined in a slit and researched phase transitions with decreasing temperature, with a fixed slit gap [18]. Gruhn and Schoen researched ellipsoids between two walls made of particles on the basis of a grand canonical ensemble and observed that ellipsoids arranged into layers sequentially, with increasing distance of the walls [19]. The interaction between a liquid crystal molecule and a wall has been also studied. Steuer *et al.* prepared two walls which had different homogeneous planar alignment and observed the twisted nematic state [20]. Barmes and Cleaver proposed an interaction between a hard anisotropic particle and a wall and investigated planar, tilted, and homeotropic states [21]. Additionally, the calculations considering the electrostatic interaction have been performed. Gwóźdź *et al.* confined ellipsoids with an electric dipole into the slit whose walls were made of fixed ellipsoids and analyzed the phase transitions [22]. Miyazaki and Yamashita applied a uniform field to the ellipsoids and observed an induced orientational transition [23]. While the static properties of confined liquid crystal molecules have been investigated widely, the dynamic properties of liquid crystal molecules confined in a slit have hardly been researched.

The purpose of the present paper is to investigate the transport properties of uniaxial nematogen Gay-Berne ellipsoids confined between two flat, structureless walls. Three kinds of transport coefficients, that is, the self-diffusion coefficient, self-rotation coefficient, and rotational viscosity will be studied. In Sec. II, the simulation cell to which the thermostat and barostat are attached, the interaction between two ellipsoids, the ellipsoid-wall interaction, and descriptions of microscopic physical quantities are described. In Sec. III, the results and discussion are presented. Static properties and the ellipsoid order are reported in the first half. Then, the dynamic properties in the ordered state are considered. The conclusion follows in Sec. IV.

*t_mima@z8.keio.jp

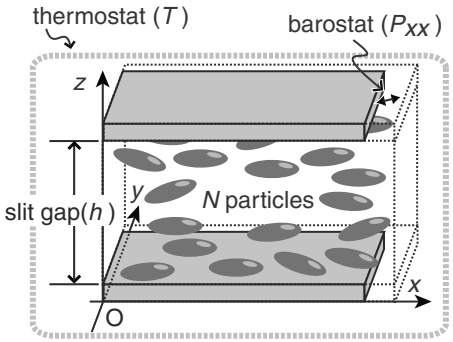

FIG. 1. Schematic figure of the system. The area of the base, A, can fluctuate so as to keep the pressure parallel to walls constant, P_{xx}. The thermostat acts for all of the ellipsoids.

II. METHODS

A. System

In order to investigate the behavior of confined, prolate, liquid crystal molecules, 16 200 uniaxial Gay-Berne ellipsoids as nematogen liquid crystals [24] were confined into a thin slit. The slit comprised two flat, structureless walls that were parallel to each other (Fig. 1). The z axis is perpendicular to the walls. First, the system is equilibrated in the $NhP_{xx}T$ ensemble, where N is the number of ellipsoids, h is the distance between two walls, and T is the temperature. $P_{xx}(=P_{yy})$ is the pressure tensor component parallel to the walls: the base area of the walls, A, fluctuates so as to keep the pressure parallel to the walls constant, P_{xx}. Then, physical quantities are calculated in the $NhAE$ ensemble, that is, the microcanonical ensemble, where E is the total energy. In this paper, h was fixed at 15, measured as the length of a short axis of the ellipsoid, and the dimensionless pressure and temperature, (P_{xx},T), were set to $(P_{\mathrm{ex}},T_{\mathrm{ex}})=(4.0,1.0)$ or $(3.0,1.0)$, which correspond to the nematic and isotropic phase individually in the bulk system [25]. We will see that ellipsoids are ordered in the high-pressure state and disordered in the low-pressure state in Sec. III. Dynamic properties were investigated only when the ellipsoids were uniaxially ordered.

B. Interaction

The interaction between two uniaxial ellipsoids was described by the Gay-Berne potential [24],

$$\phi_{\mathrm{GB}}(\boldsymbol{r}_{ij},\boldsymbol{e}_i,\boldsymbol{e}_j)=4\epsilon(\hat{\boldsymbol{r}}_{ij},\boldsymbol{e}_i,\boldsymbol{e}_j)\left[\left(\frac{\sigma_0}{r_{ij}-\sigma(\hat{\boldsymbol{r}}_{ij},\boldsymbol{e}_i,\boldsymbol{e}_j)+\sigma_0}\right)^{12}-\left(\frac{\sigma_0}{r_{ij}-\sigma(\hat{\boldsymbol{r}}_{ij},\boldsymbol{e}_i,\boldsymbol{e}_j)+\sigma_0}\right)^{6}\right], \quad (1)$$

$$\epsilon(\hat{\boldsymbol{r}}_{ij},\boldsymbol{e}_i,\boldsymbol{e}_j)=\epsilon_0\left(\frac{1}{\sqrt{1-\chi^2(\boldsymbol{e}_i\cdot\boldsymbol{e}_j)^2}}\right)^{\nu}\Psi(\hat{\boldsymbol{r}}_{ij},\boldsymbol{e}_i,\boldsymbol{e}_j,\chi')^{\mu}, \quad (2)$$

$$\sigma(\hat{\boldsymbol{r}}_{ij},\boldsymbol{e}_i,\boldsymbol{e}_j)=\frac{\sigma_0}{\sqrt{\Psi(\hat{\boldsymbol{r}}_{ij},\boldsymbol{e}_i,\boldsymbol{e}_j,\chi)}}. \quad (3)$$

Here $\boldsymbol{r}_{ij}$ is the positional vector between the ith and jth centers of mass of the ellipsoids and $\hat{\boldsymbol{r}}_{ij}$ is the normalized positional vector. $\boldsymbol{e}_i$ is the orientation vector of the ith ellipsoid, which corresponds to its long axis. The amplitude of $\boldsymbol{e}_i$ is unity. σ_0, ϵ_0, ν, μ, χ, and χ' are parameters. Ψ is the function for anisotropy,

$$\Psi(\hat{\boldsymbol{r}}_{ij},\boldsymbol{e}_i,\boldsymbol{e}_j;a)=1-\frac{a}{2}\left[\frac{(\hat{\boldsymbol{r}}_{ij}\cdot\boldsymbol{e}_i+\hat{\boldsymbol{r}}_{ij}\cdot\boldsymbol{e}_j)^2}{1+a\boldsymbol{e}_i\cdot\boldsymbol{e}_j}+\frac{(\hat{\boldsymbol{r}}_{ij}\cdot\boldsymbol{e}_i-\hat{\boldsymbol{r}}_{ij}\cdot\boldsymbol{e}_j)^2}{1-a\boldsymbol{e}_i\cdot\boldsymbol{e}_j}\right], \quad a=\chi,\chi'. \quad (4)$$

In this paper, $\epsilon_0=1$, $\sigma_0=1$. χ is set to 0.8, which corresponds to 3.0 in the axial ratio. $\nu=1$, $\mu=2$ and $\chi'=0.382$: the nematic phase can arise with this choice of parameters.

There are various descriptions of interactions between a Gay-Berne ellipsoid and a wall [18,19,22,23]. We have defined the potential by imposing anisotropy to a Lennard-Jones 9-3 potential [26]:

$$\phi_{\mathrm{wall}}(z_i,e_{i,z};z_{\mathrm{w}})=\frac{2\pi}{3}\epsilon_{\mathrm{w}}(e_{i,z})\left[\frac{2}{15}\left(\frac{\sigma_{0\mathrm{w}}}{|z_i-z_{\mathrm{w}}|-\sigma_{\mathrm{w}}(e_{i,z})+\sigma_{0\mathrm{w}}}\right)^9-\left(\frac{\sigma_{0\mathrm{w}}}{|z_i-z_{\mathrm{w}}|-\sigma_{\mathrm{w}}(e_{i,z})+\sigma_{0\mathrm{w}}}\right)^3\right], \quad (5)$$

where $e_{j,z}$ is the z component of the jth orientation and z_w is the position of the wall. As in the Gay-Berne potential, ϵ_{w}, σ_{w}, and Ψ_{w} are functions for anisotropy,

$$\epsilon_{\mathrm{w}}(e_{i,z})=\epsilon_{0\mathrm{w}}\left(\frac{1}{\sqrt{1-\chi_{\mathrm{w}}^2(1-2e_{i,z}^2)}}\right)^{\nu_{\mathrm{w}}}\Psi_{\mathrm{w}}(e_{i,z};\chi_{\mathrm{w}}')^{\mu_{\mathrm{w}}}, \quad (6)$$

$$\sigma_{\mathrm{w}}(e_{i,z})=\frac{\sigma_{0\mathrm{w}}}{\sqrt{\Psi_{\mathrm{w}}(e_{i,z};\chi_{\mathrm{w}})}}, \quad (7)$$

$$\Psi_{\mathrm{w}}(e_{i,z};a)=1-\frac{2ae_{i,z}^2}{1-a(1-2e_{i,z}^2)}, \quad a=\chi_{\mathrm{w}},\chi_{\mathrm{w}}'. \quad (8)$$

Ψ_{w} can be obtained by substituting $\boldsymbol{r}_{ij}=(0,0,z_i-z_w)$, $\boldsymbol{e}_j=(e_{i,x},e_{i,y},-e_{i,z})$ into Ψ: this condition corresponds to locating a mirror-image ellipsoid on a wall. The axial ratio for χ_w is not necessarily equal to χ as Gruhn reported [19]. On the other hand, ϵ_{w} cannot be obtained through ϵ with the mirror-image condition. Because of this definition of ϵ_{w}, the absolute value of the potential well depth increases uniformly when an ellipsoid becomes parallel to the walls. In this paper, $\sigma_{0w}=\sigma_0$, $\epsilon_{0w}=0.5$, $\chi_w=0.6$, $\nu=1.0$, $\mu=0.5$, and $\chi_w'=0.6$. The amplitude of the ellipsoid-wall interaction is of the same order as the ellipsoid-ellipsoid interaction with this choice of parameters. Figure 2 shows ϕ_{wall} curves of four configurations of a uniaxial ellipsoid. It is found that the shape of the ellipsoid-wall potential varies depending on the orientation of a uniaxial ellipsoid. Equation (5) with these parameters describes well the interaction between an ellipsoid whose

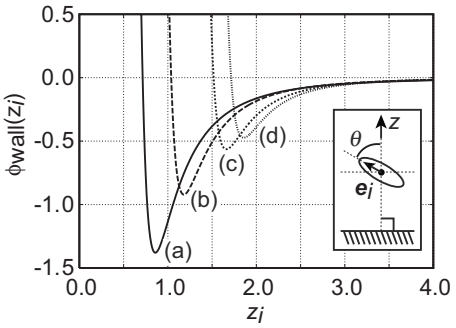

FIG. 2. Ellipsoid-wall potential. The wall is at $z_w=0$. Four conformations were drawn. θ is the angle between the orientation of a ellipsoid and z axis. (a) $\theta=\pi/2$, (b) $\theta=\pi/3$, (c) $\theta=\pi/6$, and (d) $\theta=0$.

axial ratio is 3.0 and the wall. Note that the wall described by Eq. (5) is flat and has no structure fixed on the surface. There are several definitions of the slit gap [10,18]. Considering the exclusive volumes of both an ellipsoid and a wall, first we defined Δz as the distance from the center of a wall to the surface of the wall. Δz is equal to half of the distance with which $\phi_{\rm wall}$ is zero when an ellipsoid is parallel to a wall: $\Delta z=(\sqrt[6]{2}/15)/2\simeq 0.358$. Then we defined the slit gap, h, as the distance between surfaces of two walls. With this definition, two walls are at $z_w=0$ and $z_w=h+2\Delta z$ when the slit gap is h. The spherical cutoff distance of 4.0 was applied to both potentials independent of the ellipsoid's orientation.

C. Equations of motion

When the $NhP_{xx}T$ algorithm is adopted to uniaxial ellipsoids, the total energy of the system with a thermostat and a barostat, E, is as follows [27,28]:

$$E=\sum_{i=1}^{N}\frac{\boldsymbol{p}_i^2}{2m}+\sum_{i=1}^{N}\frac{I\boldsymbol{u}_i^2}{2}+\sum_{i=1}^{N}\sum_{j>i}\phi_{\rm GB}(|\boldsymbol{q}_i-\boldsymbol{q}_j|,\boldsymbol{e}_i,\boldsymbol{e}_j)+\sum_{i=1}^{N}\phi_{\rm wall}(z_i,e_{i,z};0)+\sum_{i=1}^{N}\phi_{\rm wall}(z_i,e_{i,z};h+2\Delta z)+\frac{Q_T\xi^2}{2}+k_{\rm B}T_{\rm ex}g\ln s+\frac{Q_P\xi_P^2}{2}+P_{\rm ex}V. \quad (9)$$

Here $\boldsymbol{q}_i$ is the positional vector of the ith ellipsoid, $\boldsymbol{p}_i$ is the momentum, $\boldsymbol{e}_i$ is the orientation vector, and $\boldsymbol{u}_i$ is the time derivative of the orientation vector. ξ is the variable of the Nosé-Hoover thermostat and s is another variable of the thermostat. ξ_P is the variables of the Andersen barostat and V is the volume of the simulation cell. $T_{\rm ex}$ and $P_{\rm ex}$ are the fixed temperature and the fixed pressure, individually. m is the mass, I is the moment of inertia, and $k_{\rm B}$ is Boltzmann's constant. Q_T and Q_P are the parameters of the thermostat and the barostat, respectively, and g is the total number of degrees of freedom. The equations of motion for the ith center of mass $\boldsymbol{q}_i$ and the momentum $\boldsymbol{p}_i$ become

$$\frac{dq'_{i,\alpha}}{dt}=\frac{p_{i,\alpha}}{mA^{1/2}}, \quad (10)$$

$$\frac{dq'_{i,z}}{dt}=\frac{p_{i,z}}{m}, \quad (11)$$

$$\frac{dp_{i,\alpha}}{dt}=F_{i,\alpha}-\xi p_{i,\alpha}-\xi_P p_{i,\alpha}, \quad (12)$$

$$\frac{dp_{i,z}}{dt}=F_{i,z}-\xi p_{i,z}, \quad (13)$$

where $q'_{i,\alpha}=q_{i,\alpha}/A^{1/2}$ and α stands for x and y. The force on i, $\boldsymbol{F}_i$, is derived as $-(\partial\phi_{\rm GB}/\partial\boldsymbol{r}_i+\partial\phi_{\rm wall}/\partial\boldsymbol{r}_i)$. The equations of motion for the unit orientation vector of the ith uniaxial ellipsoid, $\boldsymbol{e}_i$, and its time derivative, $\boldsymbol{u}_i$, are applied as

$$\frac{d\boldsymbol{e}_i}{dt}=\boldsymbol{u}_i, \quad (14)$$

$$\frac{d\boldsymbol{u}_i}{dt}=\frac{\boldsymbol{G}_i}{I}-\xi\boldsymbol{u}_i-\lambda_i\boldsymbol{e}_i, \quad (15)$$

where $\boldsymbol{G}_i$ is called gorque [29], which is derived as $-(\partial\phi_{\rm GB}/\partial\boldsymbol{e}_i+\partial\phi_{\rm wall}/\partial\boldsymbol{e}_i)$. In this paper, the rotation around $\boldsymbol{e}_i$ is neglected. Lagrange multiples λ_i are imposed so as to conserve the condition $\boldsymbol{e}_i^2=1$ and $\boldsymbol{e}_i\cdot\boldsymbol{u}_i=0$. ξ and ξ_p work so as to keep the temperature to $T_{\rm ex}$ and the pressure to $P_{\rm ex}$. They are solved with s and the base area of the simulation cell, A,

$$\frac{d\xi}{dt}=\frac{1}{Q_T}[2K-gk_{\rm B}T_{\rm ex}], \quad (16)$$

$$\frac{ds}{dt}=s\xi, \quad (17)$$

$$\frac{dA}{dt}=2A\xi_p, \quad (18)$$

$$\frac{d\xi_p}{dt}=\frac{2V}{Q_P}[\mathcal{P}_{xx}-P_{\rm ex}], \quad (19)$$

where K is the momentary total kinetic energy, namely, the summation of translational and rotational kinetic energy, $\mathcal{P}_{xx}$ is the momentary pressure tensor component parallel to walls. The number of degrees of freedom, g, was set to $3N-2+2N$. The scheme of the numerical integral has been reported by Ilnytskyi and Wilson. They also reported that the difference equation yielded total energy drift. We examined and found that this drift caused the heating of the system in a microcanonical ensemble. Physical quantities were, therefore, calculated until the drift was 1% relative to $T_{\rm ex}$, and then the system was corrected by attaching the thermostat and barostat.

The results for this model are given in length, energy, mass, moment of inertia, time, pressure, and temperature units of σ_0, ϵ_0, m, I, $\sqrt{m\sigma^2/\epsilon_0}$, $\sqrt{\epsilon_0/\sigma^3}$, and $\epsilon_0/k_{\rm B}$, respectively. The time step was set to 0.005 over all simulations. The Q_T value was set between tens and hundreds and the Q_P was set to over 10 000.

D. Physical quantities

We can calculate the physical quantity profile as a function of the distance from a wall in the case of particles confined between two walls. In this paper, the system was resolved by planes parallel to the walls, then physical quantity profiles were calculated as the function of the z. The system was resolved into several thin sheets of thickness of 0.1 or 15 segments whose thickness was 1.0.

In the case of uniaxial ellipsoids, the number of the degrees of freedom of an ellipsoid is five: three translational and two rotational components. Five kinds of temperatures are, therefore, obtained from corresponding velocities, respectively. Three translational temperatures are straightforward:

$$T_\alpha(z_C) = \left\langle \frac{2}{k_B N_C} \sum_{i \in C} \frac{p_{i,\alpha}^2}{2m} \right\rangle, \tag{20}$$

where α stands for x, y, or z, C is the region of a segment, z_C is the distance from the wall representing the position of C, N_C is the number of ellipsoids in C, and $\langle\rangle$ denotes the average over samples. Two components of the rotational velocity of an ellipsoid have been obtained in a two-dimensional Cartesian coordinate perpendicular to the orientation vector of the ellipsoid. First, two unit vectors that stand for axes of the two-dimensional coordinate are defined as follows:

$$\boldsymbol{e}_{i,A} = \frac{\boldsymbol{e}_i \times \boldsymbol{e}_z}{|\boldsymbol{e}_i \times \boldsymbol{z}|}, \tag{21}$$

$$\boldsymbol{e}_{i,B} = \frac{\boldsymbol{e}_i \times \boldsymbol{e}_{i,A}}{|\boldsymbol{e}_i \times \boldsymbol{e}_{i,A}|}, \tag{22}$$

where $\boldsymbol{z}$ is the unit vector parallel to the z axis; $\boldsymbol{e}_{i,A}$ is parallel to walls, and $\boldsymbol{e}_{i,B}$ is perpendicular to walls. Second, the rotational velocity, $\boldsymbol{u}_i$, is decomposed into two components, $\boldsymbol{u}_{i,A}$ and $\boldsymbol{u}_{i,B}$:

$$\boldsymbol{u}_{i,A} = (\boldsymbol{u}_i \cdot \boldsymbol{e}_{i,A})\boldsymbol{e}_{i,A}, \tag{23}$$

$$\boldsymbol{u}_{i,B} = (\boldsymbol{u}_i \cdot \boldsymbol{e}_{i,B})\boldsymbol{e}_{i,B}. \tag{24}$$

Then the rotational temperatures become

$$T_\alpha(z_C) = \left\langle \frac{2}{k_B N_C} \sum_{i \in C} \frac{I u_{i,\alpha}^2}{2} \right\rangle, \tag{25}$$

where α stands for A or B.

For the number density profile, we have

$$\rho(z_C) = \left\langle \frac{N_C}{V_C} \right\rangle, \tag{26}$$

where V_C is the volume of C.

Two kinds of order parameter are calculated in order to investigate orientational order: P_2 and P_{2z}. P_2, commonly calculated in bulk liquid crystals, is the degree of global uniaxiality, which is the maximum eigenvalue of the following tensor:

$$\boldsymbol{Q}_2 = \left\langle \sum_{i=1}^{N} \frac{3\boldsymbol{e}_i \otimes \boldsymbol{e}_i - \boldsymbol{1}}{2} \right\rangle. \tag{27}$$

$P_2=0$ when ellipsoids are distributed at random and $P_2=1$ when ellipsoids are perfectly ordered. When $0.6 \leq P_2 \leq 0.7$, we generally regard the Gay-Berne ellipsoids as in the nematic phase in the bulk system. The eigenvector of the maximum eigenvalue is called the director, $\boldsymbol{n}$. The local order parameter, $P_2(z_i)$, can be calculated from

$$\boldsymbol{Q}_2(z_C) = \left\langle \sum_{i \in C} \frac{3\boldsymbol{e}_i \otimes \boldsymbol{e}_i - \boldsymbol{1}}{2} \right\rangle. \tag{28}$$

Local directors, $\boldsymbol{n}_C$, and their polar and azimuth angles are also calculated simultaneously. Note that we should average the matrix $\boldsymbol{Q}_2(z_C)$ when thin sheets with the thickness of 0.1 are used, rather than average eigenvalues themselves because of the problem of system size [30,31]. The local order parameter $P_{2z}(z_C)$ is sensitive to the order parallel and perpendicular to the xy plane [18]:

$$P_{2z}(z_C) = \left\langle \sum_{i \in C} \frac{(3e_{i,z}^2 - 1)}{2} \right\rangle. \tag{29}$$

$P_{2z}=-0.5$ when all ellipsoids are parallel to the walls, $P_{2z}=0$ when ellipsoids are oriented randomly, and $P_{2z}=1.0$ when all ellipsoids are perpendicular to the walls.

No value is output to profiles calculated with thin sheets where no ellipsoids were present or the number of ellipsoids was poor for sampling, in short, near the walls. Because of the aforementioned reasons, values of temperatures, P_2, P_{2z}, and the polar and the azimuth angle of the director have been not output near the surfaces of walls.

When uniaxial ellipsoids are ordered in a globally uniaxial state, transport coefficients should be calculated in appropriate director-based coordinates in every segments of the system resolved. In the present paper, profiles of the self-diffusion coefficient, self-rotation coefficient, and the rotational viscosity are calculated. Self-diffusion coefficients (SDC) as a function of the segment at C, $D(z_C)$, is calculated from the integration of the corresponding velocity autocorrelation functions (VACF), $f_{\mathrm{VACF}}(t)$. The appropriate Green-Kubo formula is

$$D_\alpha(z_C) = \int_0^{+\infty} dt f_{\mathrm{VACF},\alpha}(z_C,t), \tag{30}$$

$$f_{\mathrm{VACF},\alpha}(z_C,t) = \left\langle \frac{1}{N_C} \sum_{i \in C} v_{i,\alpha}(t) v_{i,\alpha}(0) \right\rangle, \tag{31}$$

where α stands for a component of the coordinate. VACFs should be calculated in the director-based coordinate so as to calculate SDCs when ellipsoids are in a uniaxially ordered state. The method of transformation of the coordinate or the way to define α will be explained in Sec. III.

In the case of the system of uniaxial ellipsoids, the integral of the angular velocity autocorrelation function (AVACF), f_{AVACF}, can be defined as the degree of the ease of rotational motion of ellipsoids,

$$R_\alpha(z_C) = \int_0^{+\infty} dt f_{\mathrm{AVACF},\alpha}(z_C,t), \tag{32}$$

$$f_{\mathrm{AVACF}\alpha}(z_C,t) = \left\langle \frac{1}{N_C} \sum_{i\in C} \boldsymbol{\omega}_{i,\alpha}(t)\cdot\boldsymbol{\omega}_{i,\alpha}(0) \right\rangle, \tag{33}$$

where $\boldsymbol{\omega}_{i,\alpha}=\boldsymbol{e}_i\times\boldsymbol{u}_{i,\alpha}$ is the angular velocity of the ith ellipsoid and α stands for A or B. R has no particular name, as far as the authors know. In this paper, we call R the self-rotation coefficient (SRC). In the case of ellipsoids confined in a slit, they should be calculated every component. R_A is related to the ease of the rotational motion of ellipsoids parallel to walls and R_B is related to the ease of the rotational motion perpendicular to walls.

The rotational viscosity (RV) which is defined in uniaxially ordered ellipsoids is concerned with the average rotational mobility of ellipsoids and it is important in designing and controlling liquid crystal displays. RV is related to the inverse of the integration of the director angular velocity autocorrelation function (DAVACF) [32],

$$\frac{k_\mathrm{B}T}{V_C\gamma_\alpha(z_C)} = \int_0^{+\infty} dt\langle \Omega_{C,\alpha}(t)\Omega_{C,\alpha}(0)\rangle. \tag{34}$$

Here Ω_α is a component of $\boldsymbol{\Omega}$, which is the director angular velocity vector as the external product of a director, $\boldsymbol{n}$, and its time derivative, $\dot{\boldsymbol{n}}$; $\boldsymbol{\Omega}=\boldsymbol{n}\times\dot{\boldsymbol{n}}$. Transforming the coordinate in which one axis is parallel to the director, we find that $\boldsymbol{\Omega}$ has only two components. These components are equivalent in the case of the bulk equilibrium nematic phase. In the case of uniaxial ellipsoids confined between two walls, however, we should distinguish the component parallel to walls from that perpendicular to the walls. In this paper, we have defined two director angular velocities in a similar way for the calculation of $\boldsymbol{u}_\alpha$. First, the two unit vectors that stand for axes of the two-dimensional coordinate are defined as follows:

$$\boldsymbol{e}_{C,A} = \frac{\boldsymbol{n}_C\times\boldsymbol{z}}{|\boldsymbol{n}_C\times\boldsymbol{z}|}, \tag{35}$$

$$\boldsymbol{e}_{C,B} = \frac{\boldsymbol{n}_C\times\boldsymbol{e}_{C,A}}{|\boldsymbol{n}_C\times\boldsymbol{e}_{C,A}|}. \tag{36}$$

Second, the rotational velocity of the director, $\dot{\boldsymbol{n}}_C$, is decomposed into two components, $\boldsymbol{e}_{C,A}$ and $\boldsymbol{e}_{C,B}$:

$$\dot{\boldsymbol{n}}_{C,A} = (\dot{\boldsymbol{n}}_C\cdot\boldsymbol{e}_{C,A})\boldsymbol{e}_{C,A}, \tag{37}$$

$$\dot{\boldsymbol{n}}_{C,B} = (\dot{\boldsymbol{n}}_C\cdot\boldsymbol{e}_{C,B})\boldsymbol{e}_{C,B}. \tag{38}$$

Then, two director angular velocities are calculated:

$$\boldsymbol{\Omega}_{C,\alpha} = \boldsymbol{n}_C\times\dot{\boldsymbol{n}}_{C,\alpha}, \tag{39}$$

where α stands for A or B. Finally, the rotational viscosity becomes

$$\frac{k_\mathrm{B}T}{V_C\gamma_\alpha(z_C)} = \int_0^{+\infty} dt f_{\mathrm{DAVACF},\alpha}(z_C,t), \tag{40}$$

$$f_{\mathrm{DAVACF},\alpha}(z_C,t) = \langle \boldsymbol{\Omega}_{C,\alpha}(t)\cdot\boldsymbol{\Omega}_{C,\alpha}(0)\rangle. \tag{41}$$

Note that γ_A is the rotational viscosity in the plane parallel to walls and γ_B is the other one in the plane perpendicular to walls.

Note that ellipsoids can move to other segments and might return to the original one in τ. Considering mean square displacements (MSD) every segment, we will also see that the segments with a thickness of 1.0 are acceptable in Sec. III; the MSD at the time of t in the α direction is defined every segment as follows:

$$S(z_C,t) = \left\langle \frac{1}{N_C}\sum_{i\in C} |q_{i,\alpha}(t) - q_{i,\alpha}(0)| \right\rangle. \tag{42}$$

In Sec. III, it will be reported that each segment contains more than 1000 ellipsoids; the number is sufficiently large to average. Transport coefficients profiles were calculated in the following manner. First, the simulation cell was resolved into $N_s=15$ segments parallel to the walls. Next, ellipsoids were labeled every segment at moment $t=0$. Then, autocorrelation functions were calculated from labeled ellipsoids every segment in the interval of $[0,\tau]$, where τ is the upper limit of time integration and we set τ to 4.0. Finally, the labels were updated every τ and the calculation was repeated. 7000 samples was sufficient in order to calculate SDCs and SRCs. On the other hand, up to 1 000 000 samples were demanded for the accuracy of RVs: an overlapped data collection method was applied for calculation of RVs [33].

In order to consider the difference between transport properties in the center and those that neighbor walls, Fourier cosine transforms are carried out on unnormalized correlation functions:

$$F(\omega) = \int_0^{+\infty} dt f(t)\cos\omega t, \tag{43}$$

where ω is an angular frequency, $f(t)$ is a correlation function, and $F(\omega)$ is its Fourier transform, in other words, the spectrum intensity of a cosine component with ω.

III. RESULT AND DISCUSSION

A. Static properties

To evaluate the degree of order of uniaxial ellipsoids, we now discuss static properties. Figure 3 shows three translational and two rotational temperatures in both low- and high-pressure conditions. Any temperatures are globally controlled to unity.

According to the profile of local number density and two order parameters, both the low- and high-pressure systems are categorized in two parts; one part where ellipsoids are distributed uniformly and the other part influenced by the walls. Figure 4(a) shows number density profiles in the low- and high-pressure conditions. Centers of mass of the ellipsoids appear to distribute uniformly in the center region, about $4.36\leq z\leq 11.36$, under both conditions. Uniform number density is 0.293 in the low-pressure condition and 0.322 in the high-pressure condition; these two values are in good

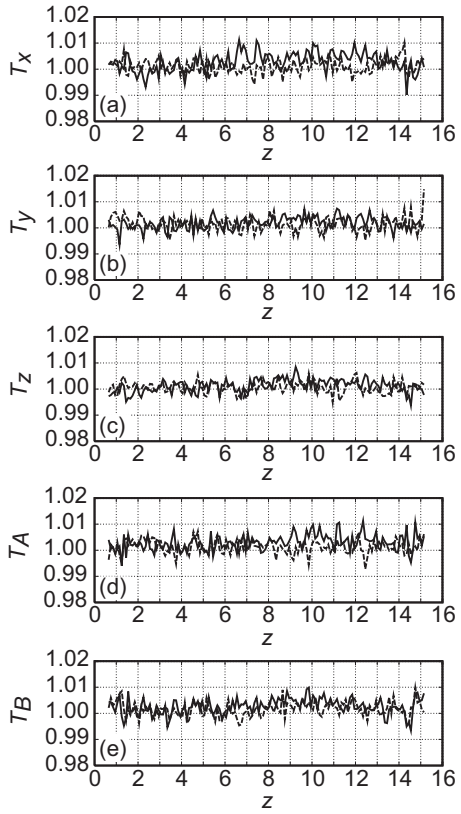

FIG. 3. Temperature profiles. Solid lines are in the high-pressure condition and dashed lines are in the low-pressure condition. Slit gap is 15. (a) T_x, (b) T_y, (c) T_z, (d) T_A, and (e) T_B.

agreement with those in bulk systems. Both profiles oscillate strongly upon approach to the walls and there are three or four local maxima near the wall. The value of the maximum is about 1.0 and the summation of thicknesses of layers near one wall is nearly equal to 4.0 of the cutoff length. This means that the centers of mass of the ellipsoids that are influenced by the walls conform to layers parallel to the wall

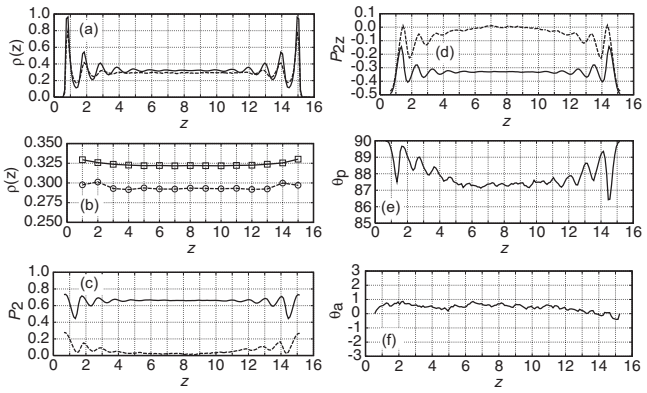

FIG. 4. Static physical quantity profiles. Solid lines (with square) are in the high-pressure condition and dashed lines (with circle) are in the low-pressure condition. (a) Number density with high resolution, (b) number density with low resolution, (c) order parameter P_2, (d) order parameter P_{2z}, (e) polar angle, and (f) azimuth angle of local director. The unit of angle is degree measure.

and seem to be ordered under both conditions. The local maxima under the low-pressure condition are smaller than those in the high-pressure condition and the local minima under the low-pressure condition are larger than those in the high-pressure condition. This difference between number densities corresponds to the difference in fluidity and packing effect. Number densities of 15 segments are, on the other hand, $0.292 \leq \rho \leq 0.301$ under the low-pressure condition and $0.322 \leq \rho \leq 0.330$ under the high-pressure condition [Fig. 4(b)]: the difference in the number of ellipsoids in every condition is not outstanding. This fact means that each segment contains more than 1000 ellipsoids and it is expected that the number of ellipsoids are sufficiently large to calculate transport coefficients every segment. Additionally, it means that if anisotropic transport is observed, it is mainly caused by the flat, structureless walls, not by the difference in the number density, namely, the thermodynamic condition.

Ordering of uniaxial ellipsoids is clarified by order parameters as in Eqs. (28) and (29). P_2 profiles are shown as in Fig. 4(c). P_2 is at most 0.3 under the low-pressure condition and about 0.03 in the center. On the other hand, P_2 values are more than 0.6 globally under the high-pressure condition: the averaged value is 0.66. It follows that confined ellipsoids are ordered with global uniaxiality. There is a part near a wall, where the value of the order parameter P_2 is under 0.6. This means that the degree of uniaxiality of ellipsoids there is weaker than another ellipsoids, in other words, orientations of ellipsoids tend to fluctuate more largely than another ellipsoids. This fact is, however, consistent with global uniaxiality because the parts with P_2 under 0.6 correspond to the local minima of a fine number density profile and the number of ellipsoids with large fluctuation is regarded to be small.

The value of P_{2z} oscillates among negative values under both thermodynamic conditions [Fig. 4(d)]. This corresponds to the ellipsoids being parallel to the walls, which is caused by the flat, structureless wall. Note that local minima of P_{2z} correspond to local maximums of number density. Under the low-pressure condition, the profile went to zero at the center. This shows that the influence of the walls exists in the center, even if the distance between walls is 15, which is over twice the cutoff length. Gruhn *et al.* have estimated that the slit gap which yields the bulk condition correctly is of the order of hundreds at least [19]. When interested in the confined particles that describe the behavior of the bulk system, one must prepare a very large number of particles. It is found that ellipsoids are not ordered globally under the low-pressure condition. On the other hand, P_{2z} under the high-pressure condition shows that ellipsoids are likely to align parallel to the walls. The value is under −0.3 globally under the high-pressure condition. In particular, local minima nearest the walls are nearly equal to −0.5. Thus it is found that ellipsoids nearest the wall orient parallel to the walls strongly. We conclude that uniaxial ellipsoids are globally ordered in $(P_{xx}, T) = (4.0, 1.0)$, as is the case in the bulk nematic phase and ellipsoids nearest the walls stratify parallel to the walls. Then, they have only translational order just near the walls in $(P_{xx}, T) = (3.0, 1.0)$ and ellipsoids are not ordered as is in the bulk isotropic phase.

In the case of the uniaxially ordered state, that is, the high-pressure state, the calculation of the local directors is

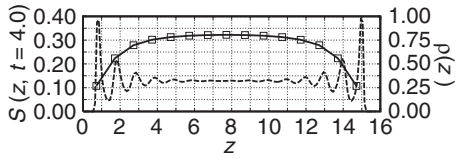

FIG. 5. Mean square displacement (MSD), S, perpendicular to walls at $t=4.0$, $S(z,t=4.0)$. MSD were calculated every 15 segments.

useful in order to consider the behavior of twist. The polar angle, θ_p, is the directional cosine angle between the ellipsoid's orientation and the z axis and the azimuth angle, θ_a, is defined between the x axis and the production of local directors on the xy plane. In the case of uniaxial ellipsoids, it is sufficient to define $0° < \theta_p < 90°$ and $-180° < \theta_a < 180°$. Those profiles are shown in Figs. 4(e) and 4(f), respectively. Figure 4(e) shows that all of the ellipsoids tend to be parallel to the walls strongly, as is shown in Fig. 4(d), and the deviation is about 3° at most. Polar oscillation near the walls corresponds to the layer structure. The azimuth angle profile shows that all of the ellipsoids tend to be oriented in one direction over the system with a deviation of only 1.0, which is not twisted greatly.

B. Dynamic properties

When transport coefficients are calculated as a profile, in other words, are calculated for every segment parallel to the walls, we should inspect whether the thickness of a segment is sufficiently large compared to the transport of ellipsoids perpendicular to segments with a given sampling time. We have to, namely, consider the MSD in the z direction at $t=\tau=4.0$. Figure 5 shows the value of the MSD perpendicular to the walls, MSD_z, at $t=4.0$ in $(P_{xx},T)=(4.00,1.00)$. The fine local number density profile is inserted there for its usefulness. All MSD_z are less than 0.33 at $t=4.0$ and MSD calculated in the nearest, second nearest, and third nearest segment are less than 0.11, 0.23, and 0.28 individually. Thus it is expected that the thickness of 1.0 for a segment is not too large for sampling by $t=4.0$ because the MSD value of 0.33 corresponds to $\sqrt{0.33} \simeq 0.58 < 1.0$ as the distance. In other words, we can define transport coefficients for every layer in $t=4.0$.

Because of the result of the azimuth profile, we are able to transform the xyz coordinate into the director-based coordinate in order to calculate VACFs of confined uniaxial ellipsoids. The manner of transformation was as follows. First, the eigenvector of the maximum eigenvalue of Eq. (27) was calculated over the system and its projection to the xy plane was defined as the new direction of coordinate, X. Z was the same as z and Y was the direction perpendicular to Z and X. In other words, the xyz coordinate was rotated around the z axis so as to transform it into the director-based coordinate. The settlement was carried out when the calculation of VACFs began. Alternatively, it was carried out at the same time of the labeling of the ellipsoids. Then, VACFs were calculated in the XYZ-coordinate system, which was fixed until $0 \le t \le \tau$: D_X, D_Y, and D_Z are calculated. Finally, the

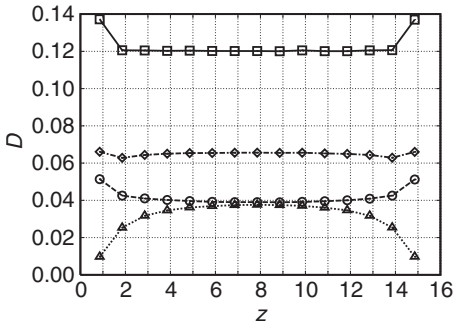

FIG. 6. Self-diffusion coefficients, D, profiles as the function of the distance from a wall. Square with solid line: D_X, circle and dashed line: D_Y, triangle with dotted line: D_Z, and diamond with dashed-dotted line: SDC averaged over three directions.

XYZ coordinate was uploaded every τ and sampling was repeated.

Generally, the SDC along the director is larger than the SDC perpendicular to the director in the bulk nematic phase [34–36]. When ellipsoids are confined between two walls, moreover, the diffusion perpendicular to the walls should be distinguished from the diffusion parallel to the walls. Therefore all three directions of the diffusion are different, as is shown in Fig. 6 in the present system.

In center, it is found that ellipsoids are three times as diffusive to the direction of the director as to the rest of the directions perpendicular to the director. The remaining two directions of diffusion are expected to be equal to each other, however, they are slightly different: the difference between D_Y and D_Z is about 0.0014. As seen in the P_{2z} profile under the low-pressure condition, this property of incompleteness for a bulk system is to be observed. The values of SDCs in the center of the current system are consistent with the result in the bulk system [37,38], two components are expected to be equal to each other with a sufficient distance between the two walls. Frenkel *et al.* have reported that the ratio of the anisotropy of diffusion, R, becomes a linear function of the global order parameter in the bulk system [39]:

$$R = \frac{D_a - D_b}{D_a + 2D_b} = P_2\left(\frac{Q^2-1}{Q^2+2}\right). \tag{44}$$

Here D_a and D_b are the self-diffusion coefficient parallel and perpendicular to the director, Q is the axial ratio and is 3.0 in the present paper. The right-hand side is equal to 0.478 from our result. When we substitute D_X to D_a and $(D_Y+D_Z)/2$ to D_b, R is 0.415. While the result of hard ellipsoids by Hess *et al.* have agreed well to the estimation, the error might tend to be greater in the case of Gay-Berne ellipsoids, that is, soft ellipsoids.

The diffusive motions near the walls are, however, very different from those in the center. Ellipsoids diffuse to the direction parallel to the walls, preferably nearest the walls. D_X increases suddenly upon approach to the segment nearest to the walls. On the other hand, D_Y increases gradually. Then, D_Z decrease gradually. SDC averaged three-dimensionally is regarded as constant over the system.

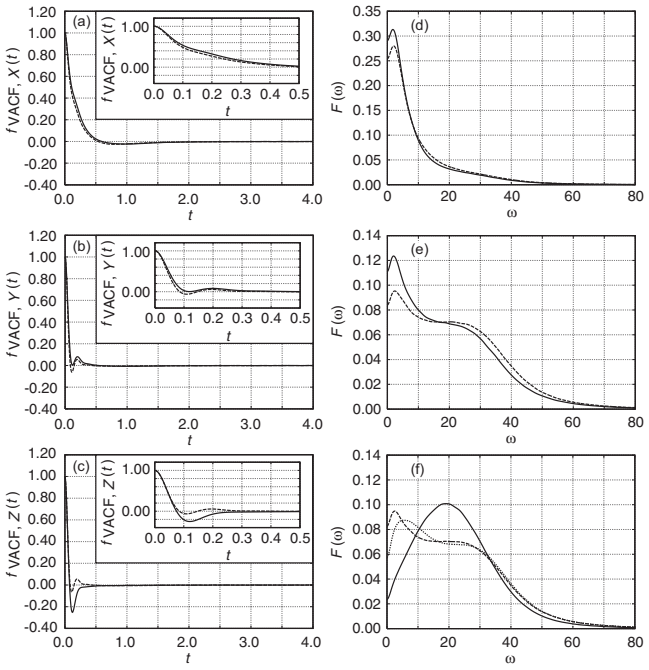

FIG. 7. Velocity autocorrelation functions (VACFs) and their spectra. (a) $VACF_X$, (b) $VACF_Y$, (c) $VACF_Z$, (d) spectrum of $VACF_X$, (e) spectrum of $VACF_Y$, and (f) spectrum $VACF_Z$. Figures of VACFs by $t=0.5$ are inserted into corresponding whole VACFs. VACFs nearest the wall at $z=0$ are shown with the solid line and those in the center are shown with the dashed line. $VACF_Z$ spectrum of the second nearest segment is shown in (f) by the dotted line.

Sharma and Woodcock have also observed such near-wall anisotropy along with a sudden increase of D parallel to walls and a gradual decrease of D_Z in the case of Lennard-Jones particles confined between flat walls [40].

In this paper, this interfacial anisotropy is explained using the analysis of VACFs and their spectra. Figure 7 shows two kinds of VACFs and their spectra: in the center and nearest the wall at $z=0$. Initial values of VACFs are equal to 1.0 in any direction over the z_C; the thermostat has controlled the translational temperature well. Then, VACFs converge to zero at $t=4.0$ with a deviation less than 0.2% of the value of $\langle v_\alpha(0)^2\rangle$. First, we focus on the behavior in the center. $VACF_X$ decays to a very shallow negative well. On the other hand, $VACF_Y$ and $VACF_Z$ look very similar: they each decay to a negative value, recover to be positive, and go to zero. Compared to $VACF_X$, both $VACF_Y$ and $VACF_Z$ decay faster and their negative wells are deeper. These behaviors cause globally larger values of D_X than D_Y and D_Z. The authors have confirmed that the shapes of VACFs in the center look very similar to those in the bulk system [37]. Observing their spectra, we have found that spectra of $VACF_Y$ and $VACF_Z$ have rich, high angular frequencies compared with that of $VACF_X$, which cause faster decay of $VACF_Y$ and $VACF_Z$. It is expected that these VACFs and their spectra in the center reflect the character of the ellipsoids themselves. Compared to VACFs in the center, on the other hand, VACFs nearest the wall are different from those in the center. $VACF_X$ nearest the wall decay more slowly than that in the center. $VACF_Y$ nearest the wall also decay more slowly and the value of the well increase to 0. These behaviors correspond to that ellipsoids near the wall diffuse in directions parallel to the walls, X and Y, more widely than in the center region. Figures 7(d) and 7(e) show that intensities of high angular frequencies of $VACF_X$ and $VACF_Y$ nearest the wall are weaker than those in the center: moreover, intensities of low angular frequencies are strengthened. We consider that this difference in diffusion is related to flat, structureless walls. Ellipsoids in the center region interact with other ellipsoids in all three directions and some interaction prevents ellipsoids from diffusing. Motive ellipsoids nearest the walls, however, have less chances of interacting with other motive ellipsoids: no ellipsoids are behind of walls. The initial decay of $VACF_X$ and $VACF_Y$, therefore, becomes slower nearest the walls. Additionally, ϕ_{wall} is a function only of z and does not influence the x and y directions explicitly. It is found that flat, structureless walls decrease the chance of interaction between motive ellipsoids, which causes the initial slow decay of $VACF_X$ and $VACF_Y$ and does not prevent ellipsoids from diffusing parallel to the walls: D_X and D_Y increase upon approach to the walls. In the case of $VACF_Z$, the depth of the well becomes deeper near the wall [Fig. 7(f)]. This behavior leads to the small value of D_z. The spectrum of $VACF_Z$ nearest the wall looks rather different from that in the center. Namely, both the peak at a angular frequency of 4.0 and the plateau around 20.0 vanish, high angular frequencies over 34 weaken, and a new peak appears at 20.0. It is expected that the new peak is caused by interaction with a wall. Because ellipsoids nearest the walls interact with the walls more frequently than ones in the center, they lose their characteristic spectrum and new spectra stimulated by the walls are realized. In order to discuss the dominant angular frequency as a function of the distance from a wall, the $VACF_Z$ spectrum of the second nearest segment is shown in Fig. 7(f). Compared to the nearest spectrum, the dominant angular frequency of the second nearest spectrum is shifted to the low angular frequency region and a plateau arises in the high angular frequency region. Ellipsoids in the second nearest segment or more center segment are enclosed by other ellipsoids and interact in various directions, therefore, intensities at 1.0 decrease and oscillations characteristic of ellipsoids are recovered. After all, the wall interacts with ellipsoids and causes the biased spectrum of $VACF_Z$, the deeper negative well of $VACF_Z$, and the decrease of D_Z.

Figure 8 shows the SRC profiles. In the center region, R_A is different from R_B: the difference between them is 0.0012. As in the same case of SDC, two values must coincide with each other when the distance between the walls is sufficiently large. We have confirmed that the center value of our SDC profile is acceptable compared with the results by de Miguel *et al.* Upon approach to the walls with a distance of 2.0, SRC varies similarly to the SDC profile: R_A increases and R_B decreases. This means that ellipsoids in the nearest and second nearest segments to the walls are easy to rotate in the plane parallel to the walls and are hard to rotate perpendicular to the walls.

In order to consider the cause of interfacial anisotropy of the rotational motion of ellipsoids near the walls, AVACFs and their spectra are investigated as is shown in Fig. 9. Simi-

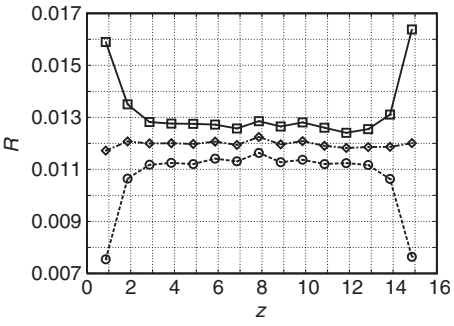

FIG. 8. Self-rotational coefficient, R, profile as the function of the distance from a wall. Square and solid line: R_A, circle and dashed line: R_B, and diamond and dashed-dotted line: R averaged.

larly to VACFs, the initial values of AVACFs both in the center and nearest the wall at $z=0$ reflect the equipartition theorem. We have confirmed that the equipartition theorem is satisfied for the rest of AVACFs. In the center, both AVACF_A and AVACF_B decay to negative wells and converge to zero more slowly than VACFs. Such behavior is consistent with the result by de Miguel *et al.* [37]. On the other hand, AVACF_A nearest the wall decay more slowly to the slightly shallower negative well compared to that in the center and the negative well of AVACF_B nearest the wall is twice as deep as that in the center. Observing of spectra of AVACFs leads to more detailed analyses. The spectrum of AVACF_A in the center has the local maximum at the angular frequency of 7.10, while the spectrum nearest the wall is more biased wholly than that in the center: the local maximum and intensities of low angular frequencies increased, and intensities of high angular frequencies decreased. The spectrum of AVACF_B has a higher maximum at a higher angular frequency and lower intensities around the maximum compared with that in the center. Similar to the case of VACFs, we think that the flat, structureless wall influences AVACFs. Remembering that the ellipsoid-wall potential is independent of $e_{i,x}$ and $e_{i,y}$, it is found that the walls do not prevent ellipsoids from rotating parallel to the walls. Additionally, ellipsoids nearest the wall have less chance of interactions with other motive ellipsoids. Their slow rotational motion, therefore, does not disturb; such a description is similar to the behavior of VACF_X and VACF_Y. As a result, the spectrum of AVACF_A in the high angular frequency region decreases, those in the low angular frequency region increase approaching the walls. Such richer intensities of low angular frequencies cause the slower initial decay of AVACF_A nearest the center: R_A increases. The flat, structureless wall is also related to R_B. Ellipsoids nearest the walls interact with their mirror-image ellipsoids frequently and have less chances of interaction with other motive ellipsoids. Then, the orientational motion of ellipsoids are strongly constrained so as to be parallel to walls; ellipsoids fluctuate more frequently. These behaviors of ellipsoids influence the local maximum of the spectrum of AVACF_B, which corresponds to the characteristic angular frequencies, so as to be strengthened at a higher angular frequency and the other intensities individually are weakened. Such biased spectrum causes the deeper negative well of AVACF_B nearest the wall: R_B decreases. It is found that the flat, structureless walls causes both translational and rotational anisotropy.

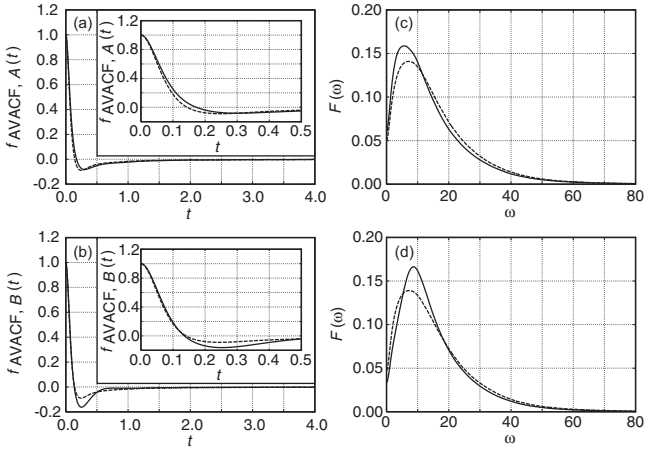

FIG. 9. Angular velocity autocorrelation functions (AVACFs) and their spectra. (a) AVACF_A, (b) AVACF_B, (c) spectrum of AVACF_A, and (d) spectrum of AVACF_B. AVACFs and their spectra nearest the wall at $z=0$ are shown with the solid line and those in the center are shown with the dashed line. Figures of AVACFs by $t=0.5$ are inserted into corresponding whole AVACFs.

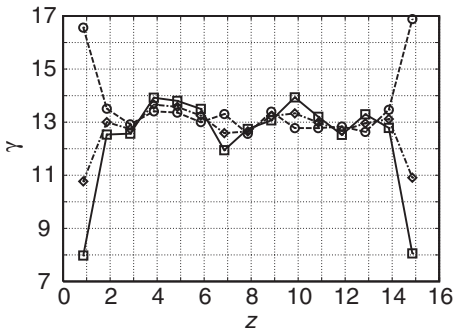

FIG. 10. Rotational viscosity (RV) profile as the function of the distance from a wall. Square and solid line: γ_A, circle and dashed line: γ_B, and diamond and dashed-dotted line: RV averaged.

Figure 10 shows the RV profiles. Our analyses has led to that the surface area, A, is 3.335×10^3: $V_C=3.335\times10^3$. In the region between $3\leq z\leq 12$, γ_A and γ_B have the large deviation. As in the same case of SDC and SRC, two values must coincide with each other when the distance between the walls is sufficiently large. The values of RVs in the center are to be compared to that calculated in the bulk system. Cuetos *et al.* have calculated the bulk RVs in canonical and microcanonical ensembles [32]. The present thermodynamic condition does not conform to their results strictly; they investigated RVs primarily in a canonical ensemble. However, we can regard the center value of the RV profile as acceptable because they also reported that the values of RVs calculated in microcanonical ensembles tended to be larger than that in canonical ensembles. Upon approach to the walls with a distance of 2.0, RV branches similarly to the SDC profile: γ_A decreased and γ_B increased nearest the walls. While the results for γ are consistent to that of R, behavior of DAVACFs themselves are different from that of AVACFs. Figure 11

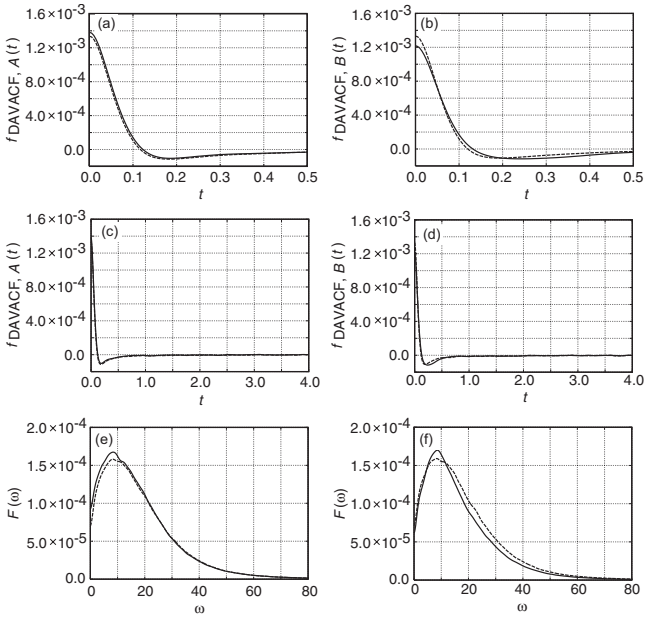

FIG. 11. DAVACFs, the director angular velocity autocorrelation functions, and their spectra. (a) DAVACF$_A$, (b) DAVACF$_B$, (c) DAVACF$_A$ by $t=0.5$, (d) DAVACF$_B$ by $t=0.5$, (e) spectrum of DAVACF$_A$, and (f) spectrum of DAVACF$_B$. DAVACFs and their spectra nearest the wall at $z=0$ are shown with the solid line and those in the center are shown with the dashed line. Figures of DAVACFs by $t=0.5$ are inserted into corresponding whole DAVACFs.

shows DAVACFs and their spectra. Both functions nearest (at $z=0$) the wall and those in the center are shown. First, the initial values of DAVACFs both in the center and nearest the wall are concentrated [Figs. 11(a) and 11(b)]. DAVACF$_A$ nearest a wall has a larger initial value than that in the center. This means that the absolute value of Ω_A nearest the walls is larger than that in the center. On the other hand, DAVACF$_B$ nearest the wall has a smaller initial value than that in the center. Such anisotropy of the initial values of DAVACFs are observed only nearest two walls and other initial values can be regarded to be equal to each other. These results of the difference of initial values do not lead to a violation of the equipartition theorem because the time derivative of the director is not a variable of the Hamiltonian: the director is just an averaged value calculated from orientation vectors of ellipsoids. Two rotational velocities of ellipsoids themselves satisfy the equipartition theorem as is shown in Fig. 3. Second, the whole shapes of DAVACFs are reviewed in Figs. 11(c) and 11(d). The behavior of the decay of DAVACF$_A$ nearest the wall looks very similar to that in the center. On the other hand, DAVACF$_B$ nearest the wall decayed more slowly to the wider negative well compared to that in the center. Then, the spectra of DAVACFs are shown in Figs. 11(e) and 11(f). All of the spectra of DAVACFs have greater angular frequencies giving respective local maxima. Intensities of the spectrum of DAVACF$_A$ increase in the low angular frequency region and hardly vary in the high angular frequency region; intensities increase on the whole upon approach to the wall. As a result, the initial value of DAVACF$_A$ increases approaching the wall. The behavior of convergence of DAVACF$_A$, however, hardly changes: γ_A decreases upon approach to the walls. On the other hand, the spectrum of DAVACF$_B$ shows that the local maximum at the angular frequency of 9.50 of the spectra grows and intensities around the maximum weakens upon approach to the wall; the intensities are weakened and biased on the whole; that causes a smaller initial value of DAVACF$_B$ nearest the wall and slower convergence from a negative well: γ_B increases upon approach to the walls. We consider that most of the consideration of AVACFs and their spectra is applicable to DAVACFs: the increase of intensities of the spectrum of DAVACF$_A$ for low angular frequencies corresponds to AVACF$_A$ and the decrease of those of DAVACF$_B$ around the local maximum corresponds to AVACF$_B$. However, the relation itself between the rotational motion of ellipsoids and that of directors might be expected complicated. Because we have observed the anisotropy of director angular velocity near the wall, nevertheless the rotational motion of ellipsoids satisfy the equipartition theorem over the system. If we do not need to calculate the rotational viscosity itself, we should remind one that the self-rotational coefficient is well-defined and preferred in order to consider the rotational motion of ellipsoids.

IV. CONCLUSION

We have investigated both static and dynamics properties of nematogen liquid crystal molecules confined between two walls. We performed constant-pressure and constant-temperature molecular dynamics simulation to Gay-Berne nematogen ellipsoids confined between two flat structureless walls. Physical quantities of temperature, number density, order parameter, self-diffusion coefficient, self-rotation coefficient, and rotational viscosity were calculated as profiles as a function of the distance from a wall.

Ellipsoids near the walls tended to be parallel to walls under both low- and high-pressure conditions: however, the global uniaxiality is observed only under the high-pressure condition.

We analyzed autocorrelation functions and their spectra so as to consider anisotropic transport behavior near walls. We concluded that the flat, structureless walls realized by the mirror-image condition caused growth of diffusion and rotation in the plane parallel to walls, strengthening of only characteristic rotational motion in the plane perpendicular to the walls, and prevention of diffusion perpendicular to the walls.

In this research, we apply the flat, structureless walls. It is possible to attach particles to the walls, when the research of a more realistic system is demanded. However, one should consider the rather expensive calculation costs when dealing with any roughness [22,41,42]. In this case, an analysis of spectra corresponding to autocorrelation functions will be useful in order to investigate the transport behavior.

ACKNOWLEDGMENTS

We acknowledge Professor M. P. Allen and Dr. D. Cheung (University of Warwick) for helpful conversations. We also

thank S. Kameoka (Keio University) for useful discussions, and Professor K. Kholmurodov (Joint Institute for Nuclear Research) and Professor K. Kurihara (Tohoku University) for conversations at the early stage of the present work. This work was supported by Grant in Aid for the 21st C.O.E. program at Keio University for "System Design: Paradigm Shift from Intelligence to Life." This research was partially supported by the Ministry of Education, Science, Sports and Culture, Grant-in-Aid for Young Scientists (B), No. 17760172, 2007.

[1] C. Alba-Simionesco, B. Coasne, G. Dosseh, G. Dudziak, K. Gubbins, R. Radhakrishnan, and M. Sliwinska-Bartkowiak, J. Phys.: Condens. Matter **18**, R15 (2006).
[2] T. Jin, B. Zalar, A. Lebar, M. Vilfan, S. Zumer, and D. Finotello, Eur. Phys. J. E **16**, 159 (2005).
[3] D. Zax *et al.*, J. Chem. Phys. **112**, 2945 (2000).
[4] R. Evans and U. Marconi, J. Chem. Phys. **86**, 7138 (1987).
[5] S. Jiang, C. Rhykerd, and K. Gubbins, Mol. Phys. **79**, 373 (1993).
[6] L. Vega, E. Müller, L. Rull, and K. Gubbins, Adsorption **2**, 59 (1996).
[7] R. Radhakrishnan and K. Gubbins, Mol. Phys. **96**, 1249 (1999).
[8] B. Coasne, J. Czwartos, K. Gubbins, F. Hung, and M. Sliwinska-Bartokowiak, Adsorption **11**, 301 (2005).
[9] K. Koga, H. Tanaka, and X. C. Zeng, Nature (London) **408**, 564 (2000).
[10] K. Koga and H. Tanaka, J. Chem. Phys. **122**, 104711 (2005).
[11] L. D. Gelb and K. E. Gubbins, Phys. Rev. E **55**, R1290 (1997).
[12] R. Radhakrishnan and K. E. Gubbins, Phys. Rev. Lett. **79**, 2847 (1997).
[13] K. Koga, G. T. Gao, X. C. Zeng, and H. Tanaka, Nature (London) **412**, 802 (2001).
[14] K. Nishio, T. Morishita, W. Shinoda, and M. Mikami, J. Chem. Phys. **125**, 074712 (2006).
[15] J. Bai, J. Wang, and X. Zeng, Proc. Natl. Acad. Sci. U.S.A. **103**, 19664 (2006).
[16] M. Whitby and N. Quirke, Nature (London) **2**, 87 (2007).
[17] B. Coasne, S. K. Jain, and K. E. Gubbins, Phys. Rev. Lett. **97**, 105702 (2006).
[18] G. D. Wall and D. J. Cleaver, Phys. Rev. E **56**, 4306 (1997).
[19] T. Gruhn and M. Schoen, Phys. Rev. E **55**, 2861 (1997).
[20] H. Steuer, S. Hess, and M. Schoen, Phys. Rev. E **69**, 031708 (2004).
[21] F. Barmes and D. J. Cleaver, Phys. Rev. E **71**, 021705 (2005).
[22] E. Gwozdz, K. Pasterny, and A. Brodka, Chem. Phys. Lett. **335**, 71 (2001).
[23] T. Miyazaki and M. Yamashita, Mol. Cryst. Liq. Cryst. Sci. Technol., Sect. A **347**, 189 (2000).
[24] J. Gay and B. Berne, J. Chem. Phys. **74**, 3316 (1981).
[25] E. de Miguel and C. Vega, J. Chem. Phys. **117**, 6313 (2002).
[26] T. Hill, J. Chem. Phys. **16**, 181 (1948).
[27] W. G. Hoover, Phys. Rev. A **31**, 1695 (1985).
[28] J. Ilnytskyi and M. Wilson, Comput. Phys. Commun. **134**, 23 (2001).
[29] M. Allen and D. Tildesley, *Computer Simulation of Liquids* (Oxford University Press, New York, 1987).
[30] R. Eppenga and D. Frenkel, Mol. Phys. **52**, 1303 (1984).
[31] E. de Miguel, Phys. Rev. E **47**, 3334 (1993).
[32] A. Cuetos, J. Ilnytskyi, and M. Wilson, Mol. Phys. **100**, 3839 (2002).
[33] D. Rapaport, *The Art of Molecular Dynamics Simulation* (Cambridge University Press, Cambridge, England, 2004).
[34] S. Cozzini, L. Rull, G. Ciccotti, and G. Paolini, Physica A **240**, 173 (1997).
[35] M. P. Allen, Phys. Rev. Lett. **65**, 2881 (1990).
[36] S. Dvinskikh and I. Furó, J. Chem. Phys. **115**, 1946 (2001).
[37] E. de Miguel, L. F. Rull, and K. E. Gubbins, Phys. Rev. A **45**, 3813 (1992).
[38] S. Sarman and D. Evans, J. Chem. Phys. **99**, 620 (1993).
[39] S. Hess, D. Frenkel, and M. Allen, Mol. Phys. **74**, 765 (1991).
[40] S. Sharma and L. Woodcock, J. Chem. Soc., Faraday Trans. **87**, 2023 (1991).
[41] D. Cheung and F. Schmid, J. Chem. Phys. **122**, 074902 (2005).
[42] K. Kiyohara, K. Asaka, H. Monobe, N. Terasawa, and Y. Shimizu, J. Chem. Phys. **124**, 034704 (2006).